

RESEARCH ARTICLE

Polymer
COMPOSITES

WILEY

Computational and experimental study on the resistance welding process of a glass fiber-reinforced epoxy-based composite with thermoplastic interlayer adherent

Yunhao Liang^{1,2} | Yu Shi¹

¹Leeds Institute of Textiles and Colour (LITAC), School of Design, Woodhouse Lane, University of Leeds, UK

²The Department of Physical, Mathematical and Engineering Sciences, University of Chester, Chester, UK

Correspondence

Yu Shi, Leeds Institute of Textiles and Colour (LITAC), School of Design, Woodhouse Lane, University of Leeds, LS2 9JT, UK.

Email: y.shi2@leeds.ac.uk

Funding information

UK Research and Innovation; HORIZON EUROPE Framework Programme

Abstract

In this work, resistance welding of a glass fiber-reinforced epoxy composite (GFRC) was studied with numerical optimization and experimental validation. A steel mesh and polymethyl methacrylate (PMMA) films were used as the heating element and adherent interlayers, respectively. A transient heat transfer module was implemented to conduct the parametric optimization study, with variables of electricity power, clamping distance and weld time. The optimal welding condition was then confirmed as 20 W, 0.4 mm and 30 s, with a melting degree of 95.2%. A thermal meter and a thermal camera validated the simulated temperature results. Welding quality was experimentally characterized by single lap shear tests and scanning electron microscopy (SEM). The highest lap shear strength of 3.8 ± 0.3 MPa was captured on the specimen welded with the optimized condition. This was 76% that of the benchmark made with the adhesive bonding method but it was over 200 times faster.

Highlights

- Resistance welding of GFRC with PMMA films and a steel mesh is studied with FEA.
- Simulation results are quantitatively validated with experimental methods.
- Optimal welding conditions are confirmed in association with welding tests.

KEYWORDS

glass fiber-reinforced epoxy composite, polymethyl methacrylate, resistance welding, simulation, validation

1 | INTRODUCTION

Continuous fiber-reinforced polymer-based composites (CFRC) have been gaining increasing interest from researchers and engineers, due to their outstanding properties and the high potential for high-performance applications, especially the specific high strength compared to

traditional structural materials.^{1–6} However, in the manufacturing industry the fabrication of large pieces of composites with sophisticated geometry is limited, giving rise to the requirement for efficient joining and bonding of CFRC parts, as well as in the repairing industry. There have been three major joining technologies, including mechanical fastening, traditional adhesive and fusion

This is an open access article under the terms of the [Creative Commons Attribution](https://creativecommons.org/licenses/by/4.0/) License, which permits use, distribution and reproduction in any medium, provided the original work is properly cited.

© 2024 The Authors. *Polymer Composites* published by Wiley Periodicals LLC on behalf of Society of Plastics Engineers.

bonding. However, there are inevitable shortcomings in the mechanical fastening and the adhesive bonding techniques. For the former, machining such as drilling can damage the composite while it consumes the additional tools (e.g., drill bits). The adhesive bonding is reported to be labor intensive with a long curing time.⁷

Fusion bonding, also known as welding, has been widely used for joining metals, with huge potential to join composites as it requires a shorter processing cycle and an easier operational setup. It usually consists of the following steps: heating up the weld line to above either the glass transition temperature (T_g) for amorphous or the melting temperature (T_m) for crystalline/semi-crystalline thermoplastics with a proper pressure applied during diffusion of molecules and consolidation of joint; Cooling down to the room temperature to solidify the polymer. Depending on the heating source, different welding approaches have been reported, including hot-press welding,^{8–10} ultrasonic signal welding,^{11–13} laser welding,^{14,15} induction welding¹⁶ and resistance welding.¹⁷ Although they are faster than the adhesive bonding, most of them are either high-cost or limited to bond large-scale components, such as the laser and the ultrasonic welding.^{11,12} In comparison, the resistance welding can be a fast (of the order of seconds to minutes) and inexpensive way with less dependency on equipment and high potential to perform autonomously.⁷ Furthermore, the heating element being used in resistance welding usually remains in the joint interface, giving the possibility of disassembly and rewelding for repair purposes.¹⁸

Resistance welding has been reported to join thermoplastics-based composites reinforced by continuous glass or carbon fibers.^{18–21} Experimental and computational techniques have been conducted by using single lap shear tests to characterize the welding quality and the finite element analysis (FEA) to simulate the heat transfer within composite joints during welding processes.^{22,23} The effect of welding parameters, such as electricity power, clamping distance, resistance of heating element, and welding pressure, has been widely investigated. However, the simulation of the resistance welding process for joining thermoset-based composites with thermoplastics and the study on the validation of the simulation results are rarely reported. This is significantly important not only for manufacturing and assembly, but also for repairing thermoset-based composites to facilitate the sustainability with extended life cycles, such as in the wind energy industry.^{24,25} It has been proven that PMMA can be completely miscible with epoxy monomers,²⁶ and the formation of physical interaction (hydrogen bonding) between carbonyl groups of PMMA and hydroxyl groups of epoxy resin has been determined with infrared

spectroscopy.²⁷ Therefore, it has the huge potential to act as the interlayer bonding material to bond epoxy-based composites via resistance welding techniques.

This study is to explore the application of Elium[®]28 PMMA interlayers in the resistance welding process of a glass fiber-reinforced epoxy composite with a fully designed experimental setup and computational modeling. The effect of parameters governing the welding process, including electricity power, clamping distance and welding time is numerically studied to find out the optimal welding condition. The heat transfer during welding is quantitatively and qualitatively assessed by a thermal meter system and a thermal camera system. Single lap shear tests are performed to evaluate the welding strength as a quality assessment. The outcomes have demonstrated the developed numerical model can be applied to predict and optimize the composite welding, and that the joining method can be implemented to bond the thermoset composite by the thermoplastic PMMA resins.

2 | MATERIALS AND METHODS

2.1 | Materials

The glass fiber epoxy prepreg (VTC401-G290T-42%RW-1280 SHD0323, SHD Composite Materials Ltd., UK) was applied to make the substrate composites to be welded, also known as the adherend. A 304-grade steel mesh was selected, with a wire diameter 30 μm , an opening width 100 μm and a thickness 50 μm (see Figure 1A), as the heating element. Meanwhile, a PMMA film (Figure 1B) was manufactured from a liquid three-component resin (Elium[®] 191 O/SA, Arkema S.A., Europe) as the additive interlayer to bond the thermoset-based composite substrates.

2.2 | Fabrication of composites and PMMA films

The glass fiber-reinforced epoxy composites consist of six plies with a thickness of about 2 mm after curing. A bridge saw (PRO Bridge Saw, Vitrex) was used to trim and cut the fabricated GFRC plates into the geometry of 101.6 mm * 25.4 mm designed for single lap shear testing, as per ASTM D1002.²⁹

To bond the thermoset composites by welding, a thermoplastic PMMA film was fabricated using Elium[®] 191 O/SA mixture with the resin (48.5 wt%), accelerator (48.5 wt%) and initiator (3 wt%). The liquid mixture was degassed at 0.1 Bar for 20 min to remove air bubbles, which was then sandwiched by two glass plates (25.4 mm * 76.2 mm) with coverslips inserted at the two sides to

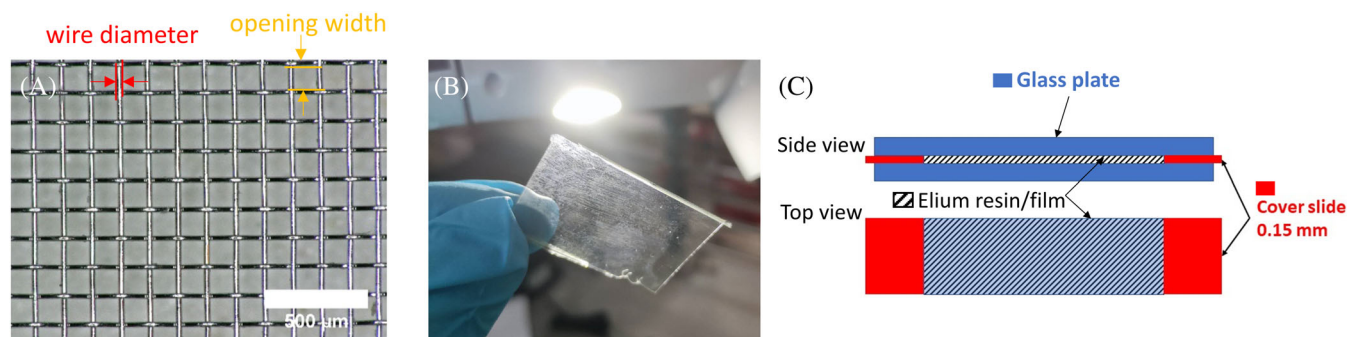


FIGURE 1 (A) Optical microscopic image of the steel mesh, (B) photo of the fabricated PMMA film and (C) schematic graph of the setup for the fabrication of PMMA films.

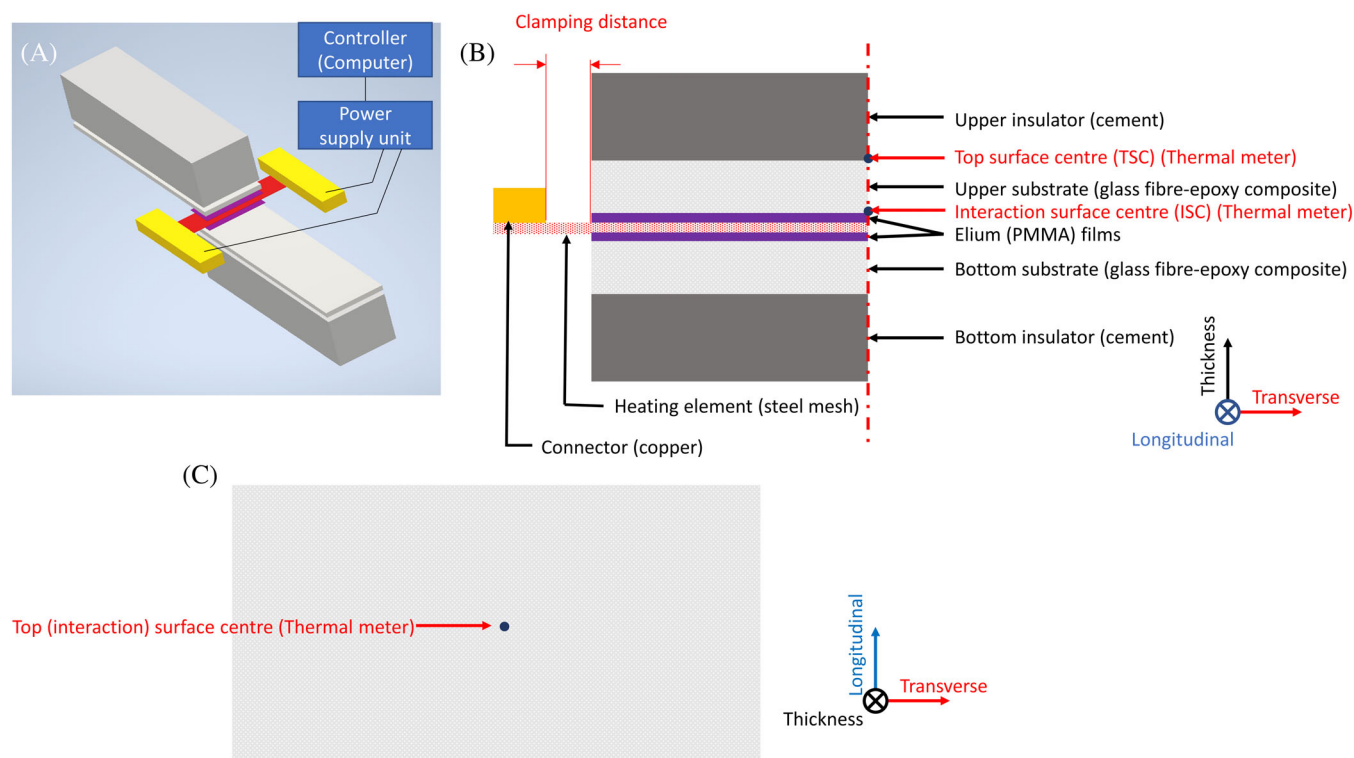


FIGURE 2 (A) Schematic of a fully assembled resistance welding setup, where the yellow, gray, white, red and purple parts represent copper connectors, cement insulators, GFRC adherents, heating element (a steel mesh) and PMMA films, respectively; (B) the cross-section of half the welding section with the global coordinate system and the locations of the two points of which the temperature is detected by the thermal meter; (C) top view of the welding section further showing the temperature measurement positions.

function as spacers, see Figure 1C. The achieved film was 0.15 mm thick, enough to fill the gaps at the interface between the adherents. The films were cured at 20°C for 18 h with a post curing process at 80°C for 1 h, advised by the supplier.

2.2.1 | Resistance welding setup

The setup used for the resistance welding process consisted of a computer controller, a power supply unit (EA-PS

5040-40A, EA ELEKTRO-AUTOMATIK GMBH & CO, Germany) and the welding assembly, indicated in Figure 2A. To design the welding tests, a block of cement insulator, the glass fiber reinforced composite adherends, layers of PMMA films and a steel mesh as heating element were constructed from exterior to interior, as shown in Figure 2B.

The dimensions of the welding assembly were controlled according to the ASTM D1002,²⁹ the overlap area was 12.7 mm * 25.4 mm. The glass fiber composite adherends were mechanically sanded with sandpaper (SiC-paper #1000, Struers, UK) to increase the surface

roughness for an improved bonding quality. In addition, a contact pressure of about 0.2 MPa was applied on the top of the welding assembly, which enabled the intimate contact between different parts without being overapplied. Furthermore, this pressure also complied with the assumptions of no displacement and perfectly intimate contact applied in the numerical modeling below. To explore the effect of clamping distance on the welding quality, the clamping distance was controlled within the range from 0 to 1.1 mm.

2.2.2 | Numerical simulation

The numerical modeling of the resistance welding process was developed based on the Joule heat effect. The transient heat transfer and the phase change of the thermoplastic material were investigated by the commercial FEA software, COMSOL Multiphysics. The energy (E) generated through the Joule heat effect can be expressed by the equation below:

$$E = I^2 R t, \quad (1)$$

where I , R and t measure the current through the heating element, resistance of the heating element and the welding time, respectively. All materials used in the simulation were macroscopically isotropic, except the composite adherends. The displacements during the resistance welding process caused by pressure and melting of polymers were not considered³⁰ in the model, therefore, only the Heat Transfer and AC/DC (Joule Heating) modules were used. The heat required for welding was provided by the Joule heating effect from the heating element, i.e. the steel mesh. The transient heat transfer is governed by:

$$\frac{\rho C_p \partial T}{\partial t} - \nabla \cdot (k \nabla T) = Q, \quad (2)$$

where ρ , C_p , T , k and Q measure the density, specific heat capacity, temperature, thermal conductivity and heat generated from the heating element, respectively. The boundaries of the model were set with free

convection and surface-ambient radiation. For the thermal convection coefficient (h) of all the external surfaces exposed to air, it was controlled as a constant of $5 \text{ W/m}^2\text{K}$.³¹ The ambient temperature (T_{amb}) was set to be 20°C and the convective heat transfer, q_c , can be described by

$$q_c = h(T_{\text{amb}} - T). \quad (3)$$

Regarding to thermal radiation, most of the organic surfaces have a surface emissivity close to 0.95, in this simulation, the surface emissivity (ϵ) was hence set to be 0.95,³² representing that all materials involved in the welding process were assumed to be thermal black bodies. This applied to all the surfaces exposed to the ambient environment, and the heat transferred through radiation, q_r , can be calculated with the Stefan-Boltzmann constant, σ , via the equation:

$$q_r = \epsilon \sigma (T_{\text{amb}}^4 - T^4). \quad (4)$$

Because PMMA is an amorphous material, the latent heat of melting and fusion was neglected.^{30,32} The contact of different parts was perfectly intimate, and all the materials properties were assumed to be independent of temperature.

The properties of different materials inputted into the simulation, which were assumed to be macromorphologically isotropic, are listed in Table 1.

However, in terms of the GFRC, as most of the composites were defined as orthotropic in numerical model,³⁸ the in-plane thermal conductivity was measured by a thermal conductivity meter (MP-2, Thermtest Inc., Canada), but the through-thickness thermal conductivity was not measurable due to the equipment limitation. Therefore, it was analyzed in two cases: the same as the in-plane one (isotropic), 0.34 W/m/K , and the value (k_c) calculated as 0.634 W/m/K , using the parallel model of the rule of mixtures with the volume fractions for reinforcement (v_r) and matrix (v_m) via the equation below:

$$k_c = v_r * k_r + v_m * k_m \quad (5)$$

TABLE 1 Properties of the isotropic materials used for the Joule heating simulation in COMSOL.

Material	Density (kg/m ³)	Thermal conductivity (W/m/K)	Specific heat capacity (J/kg/K)	Electrical conductivity (S/m)
Insulator ³³	1750	0.5	880	0
Elium® film ^{34,35}	1170	0.19	1260	0
Heating element ^{36,37}	3765	6.27	646	1.3×10^5

TABLE 2 Properties of the GFRC applied in the simulation.

Property	Density (kg/m ³)	In-plane thermal conductivity(W/m/K)	Through-thickness thermal conductivity (W/m/K)	Specific heat capacity (J/kg/K)	Electrical conductivity (S/m)
Set 1	1676	0.34	0.634	924	0
Set 2	1676	0.34	0.34	924	0

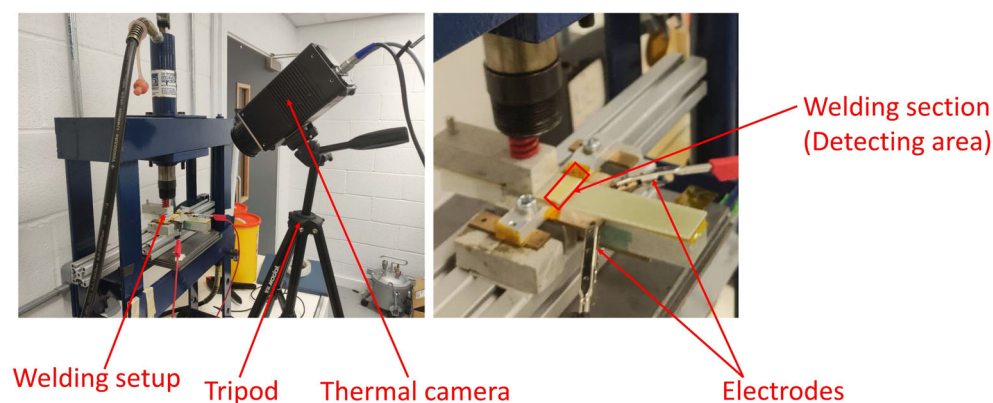


FIGURE 3 Thermal camera setup used to qualitatively detect the temperature distribution at the welding section.

where k_r and k_m measure the thermal conductivities of the glass fiber and epoxy whose values referred to the literature.³⁸ The volume fractions were found from the manufacturers' guide, $v_r = 40\%$ and $v_m = 60\%$, which was further confirmed by TGA. The sets of properties of GFRC applied in modeling are tabulated in Table 2. The isotropic analysis of the GFRC properties can be found in Figure S1.

For the meshing process, free quadrilateral was selected as the mesh element, whose optimized size was confirmed to be 1 mm through the mesh convergence analysis involved in Data S1. The results for the mesh convergence are shown in Figure S2.

2.3 | Characterizations and experimental tests

2.3.1 | Thermogravimetric analysis

The thermal properties of the PMMA films and the GFRC were measured with a thermogravimetric analysis (TGA) machine (TGA 550, TA, USA). The samples (ca 20 mg) were tested in a nitrogen atmosphere with a flow rate of 40 mL/min and a ramping speed of 25°C/min. The temperature range was set from 30 to 650°C. For GFRC, after the ramping process, the purging gas was changed from nitrogen to air, followed by an isothermal stage at 650°C for 10 min, where the final residual weight was attributed to the glass fiber loading rate. The TGA results and discussion can be found in Figure S3.

2.3.2 | Experimental validation of the simulation results

Two techniques, a dual-channel thermal meter (RSPRO 1316, RS Components Ltd., UK) and a thermal camera (VarioCAM HD head, InfraTec GmbH, Germany), were used to quantitatively and qualitatively validate the temperature results of the welding processes simulated in COMSOL Multiphysics, respectively.

The temperatures at two designated points were measured with the thermal meter, see Figure 2A,B. One was located at the top surface center of the welding area on the upper substrate, which is referred to as the top surface center (TSC). Another one was placed at the center of the interface between the top substrate and the top Elium[®] film, namely the interaction surface center (ISC). The results were quantitatively compared with those from the simulation.

For qualitatively validating the simulation results, temperature maps were obtained from the thermal camera setup shown in Figure 3, processed with the manufacturer's software "IRBRS3 professional."

2.3.3 | Single lap shear test

To characterize the resistance welding quality, single lap shear tests were implemented on the joint samples following the ASTM D1002.²⁹ Meanwhile, a benchmark sample was made via the conventional adhesion method, with the liquid Elium[®] resin as the adhesive, following

the geometry requirement and sample preparation procedure stated in the ASTM D1002.²⁹ For each welding condition, at least three specimens were measured, and the average lap shear strength and its standard uncertainty were calculated. The lap shear strength, τ , was calculated via the following equation:

$$\tau = \frac{F_{\max}}{L_0 * W}, \quad (6)$$

where F_{\max} , L_0 and W measure the maximum load during the test, the original length of the overlap area and the width of the overlap area, respectively.

2.3.4 | Scanning Electronic Microscopy

A scanning electronic microscope (TM3030 Plus, HITACHI, Japan) was used to investigate the micromorphology of the fracture surfaces of the welding samples after single lap shear tests, under energy dispersive x-ray analysis (EDX) observation mode with the accelerating voltage of 15 kV and magnifications of 100 and 400 times. The obtained images were used to analyze the fracture mechanism of the sample welded with the optimum condition in comparison to the benchmark sample.

3 | RESULTS AND DISCUSSION

3.1 | Parametric optimization of the welding process with the assistance of COMSOL multiphysics

The welding process was simulated with the transient heat transfer FEA model, where three variables were considered during the optimization process, including electricity power, clamping distance (refer to Figure 2B) and welding time. The primary discipline for the optimization is to improve the temperature distribution through controlling the edge effect during the welding process. The edge effect is caused by the poor heat transfer from the heating element into the ambient through natural convection as opposed to that caused by conduction within the welding stack. This difference results in significantly large thermal gradients at the edges, giving rise to fast melt front propagation in that area, which can cause severe thermal stress and local overheating/material degradation.³⁹ The optimization was following the below processes: to start with, electricity power ranging from 10 to 30 W with an interval of 5 W was chosen for the transient model with a fixed clamping distance of 0.5 mm to minimize the edge effect. The clamping

distance values were then varied between 0 and 2 mm under the optimal electricity power confirmed from the previous step, so as to further minimize the edge effect and meanwhile maximize the safe processing window. The calculated melting level of the thermoplastic adherent-Elum[®] films was used to determine the optimal welding conditions.

To choose the optimal welding power, the temperature along the red line shown in Figure 4A was detected, where the observed plane is the interface between the upper substrate and the upper Elum[®] film, and red line is in the middle of the joint area (blue) on the same plane. The edge effect during welding process can be monitored with the temperature distribution along the line as shown in Figure 4. There were three types of temperature distribution observed along the red line, within the measured powers: (1) when it was in the beginning of the welding process, along the red line, the temperature at the two ends was higher than that in the middle, especially at relatively low powers and early welding stages, that is, 10 W at 10 s (Figure 4B); (2) the temperature at the two ends was lower than that at the middle, which was dominant at relatively high powers and late welding stages such as 30 W at 60 s (Figure 4D); (3) the temperature was more evenly distributed than the previous two with smaller derivations where the edge effect was minimized. Therefore, the type (3) is practically ideal during the welding process. For different powers, the average temperature of type (3) and the time when type (3) reached were depicted in Figure 4E. It is found that the type (3) average temperature increased with the increase of electricity power, while the type (3) reaching time showed an opposite tendency. The effectiveness of increasing power on shortening the type (3) reaching time decreased as the power increased, which can be measured by the ratio of time reduced to power increased, for example, the slope from 40 to 30 s was 1 s/W lower than that of other periods, 2 s/W, shown in Figure 4E.

Upon comparison, the optimum welding power was defined as 20 W with the type (3) average temperature of 244°C which was lower than the degradation temperature of PMMA shown in Figure S3. Furthermore, the welding process with 20 W was faster to reach type (3), at 40 s, than that with 15 W, at 50 s. Therefore, the electricity power of 20 W was defined as the optimal power for the welding process.

To further increase the temperature distribution-minimize the edge effect, and to increase the processing safety by maximizing the processing window, the effect of clamping distance on the temperature distribution at the joint area was investigated numerically. The average temperatures along the edge and the middle line of the joint area were simulated, whose locations are indicated

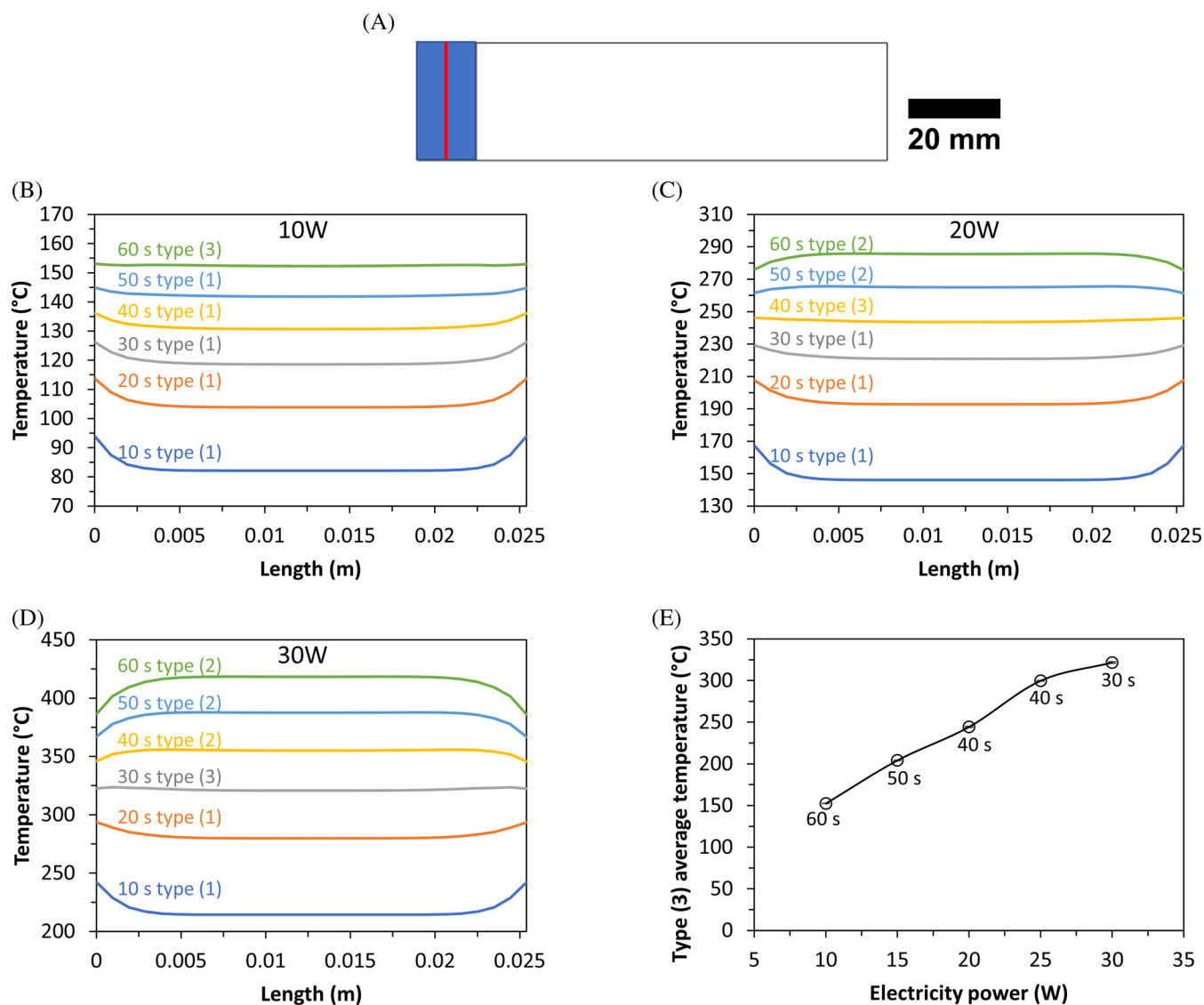


FIGURE 4 (A) Interface between the upper substrate and the upper Elium[®] film of the welding assembly where the blue area shows the joint area and the red line is the middle line along transverse direction (referring to the coordinate system in Figure 2) of the joint area; (B–D) plots of temperature against the length along the red line for different electricity powers and welding times and; (E) type (3) average temperature versus electricity power on which the welding time is indicated, and the solid line provides a guide for the eye.

with the orange and black lines in Figure 5A, respectively. The dependence of temperature on the welding time under different clamping distances is plotted in Figure 5B–D.

The results shown in Figure 5B–D indicate that for the average temperatures along both the edge and the middle lines, an increase was seen as the welding time increased. To quantify the processing safety, the processing window was measured and defined as the period between the melting temperature (180°C) and the degradation temperature (250°C) of the PMMA film. The processing window was 18 s at the clamping distance of 0 mm and increased to 32 s at 0.4 mm, followed by a decrease to be 0 s at 2 mm, see Figure 5E. Thereafter,

degradation was detected at high temperature regions before low temperature regions melted. The largest processing window was determined to be 32 s when the clamping distance was 0.4 mm at 20 W.

To determine the optimal welding time, the melting degree (φ) expressing the surficial melting degree was used, which can be calculated through the equation below:

$$\varphi = \frac{S_m}{S_t} * 100\%, \quad (7)$$

where S_m and S_t measure the surface area with the temperature above 180°C and the total area of the target

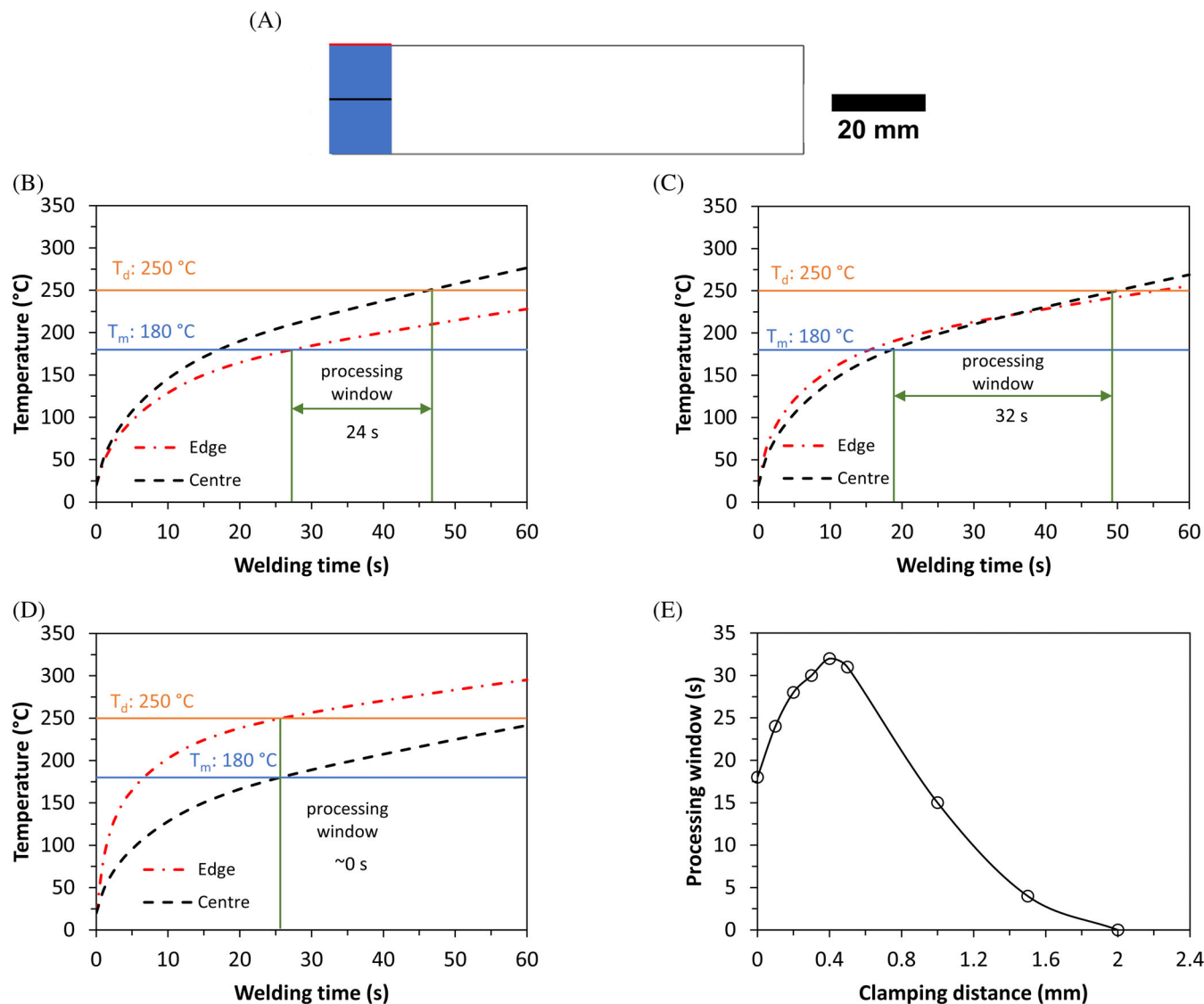


FIGURE 5 (A) the interface between the upper substrate and the upper Elum[®] film, where the joint surface is marked in blue, and the orange line and the black line indicate the temperature detection location along the edge and the middle lines (longitudinal direction), respectively; (B–D) show the average temperature along the two lines against the welding time with different clamping distances at 20 W and; (E) how the processing window changes with the clamping distance, where the line provides a guide for the eye.

surface (the blue region in Figure 5A), respectively. The dependence of melting degree on the welding time and the temperature distribution maps at the interested surface are shown in Figure 6.

Figure 6A shows that at early stages, a plateau was seen at zero melting degree on the target surface. However, when it reached 15 s, a sudden increase in the melting degree of over 80% appeared, followed by another plateau at 95.2%, 30 s (here we treat the melting degree over 95% as the goal for the welding purpose). There was an increase of 3.1% from 30 s until the PMMA films started thermal degradation (above 250°C), see the red circles in Figure 6A, of which the period is considered as the safe processing window. This phenomenon suggests

that the optimal welding time was 30 s with a proper process window of about 10 s.

The temperature maps shown in Figure 6B also depict that the melting degree kept being zero in the beginning of the welding process. After 30 s of welding, the joint surface was nearly fully filled with the dark red color, giving the melting degree of 95.2% on the target surface according to Figure 6A. Therefore, in terms of high efficiency, the optimal welding time was preliminarily defined to be 30 s for the welding process with the clamping distance and power to be 0.4 mm and 20 W, respectively. To validate the simulation results, experimental measurements were implemented, of which the results are analyzed below.

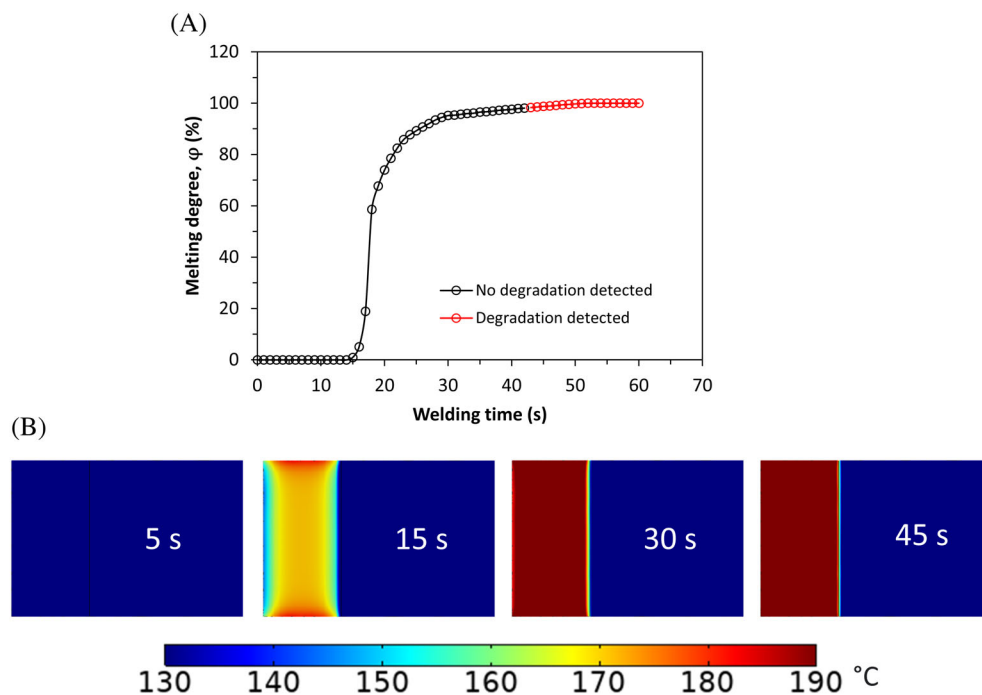


FIGURE 6 Evaluation of the joint surface between the upper substrate and the upper Elium[®] film upon the welding process with the clamping distance of 0.4 mm and the power of 20 W by (A) the plot of melting degree versus welding time, and (B) the temperature maps at different welding times; The solid line in (A) provides a guide for the eye.

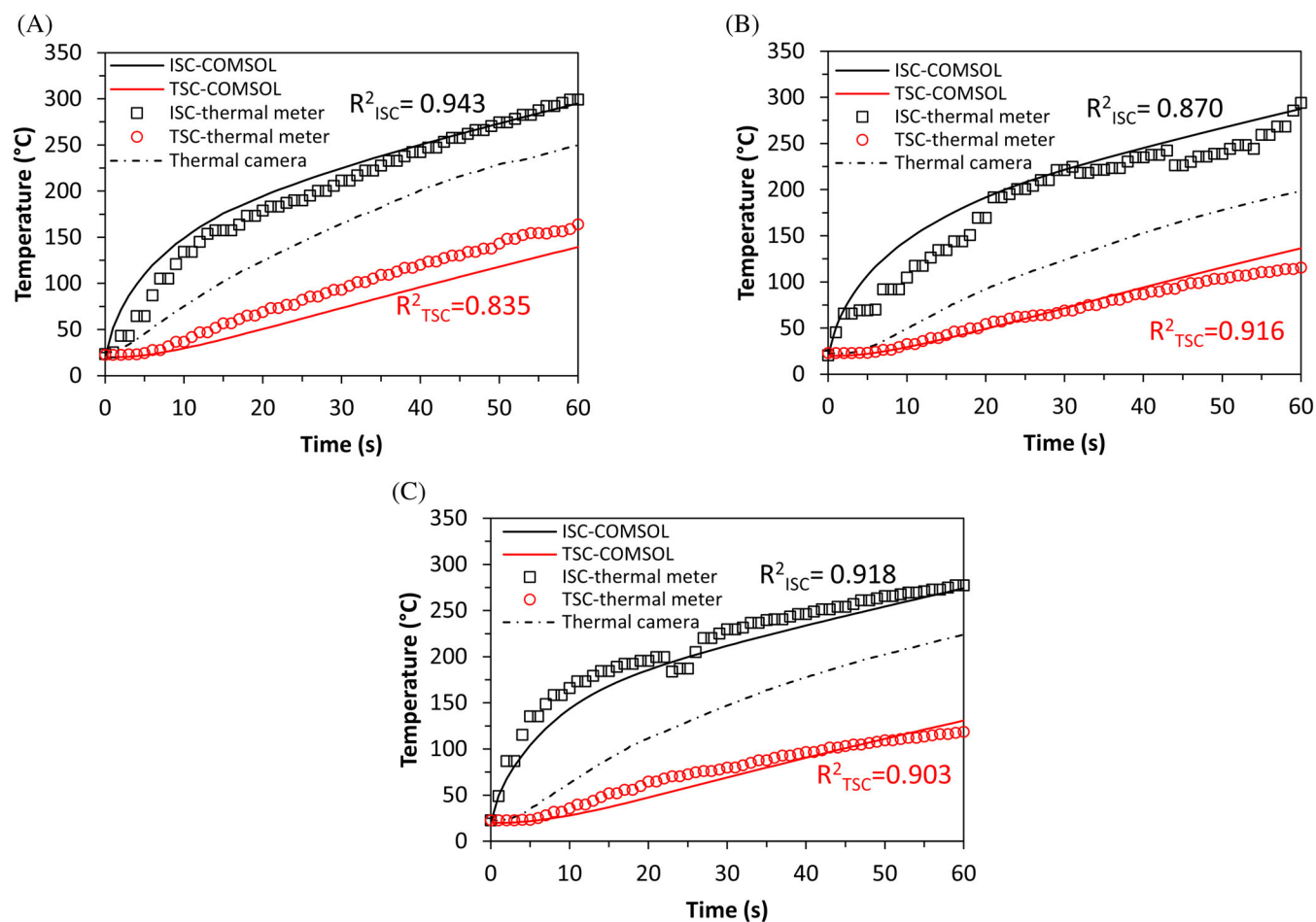


FIGURE 7 Dependence of temperature on the welding time at 20 W with three clamping distances, (A) 0.001 mm (zero in reality), (B) 0.4 mm and (C) 1.1 mm, where the solid lines and dash-dot lines indicate the results from simulation and the thermal camera respectively, and the open symbols represent the results from the thermal meter; R^2 is the determination coefficient.

3.2 | Quantitative and qualitative measurement of the temperature and its distribution

To both quantitatively and qualitatively validate the simulation results, a thermal meter and a thermal camera were used to detect the evolution of temperature during the welding processes with different clamping distances, respectively. Three clamping distances (0.001, 0.4 and 1.1 mm) were applied with a fixed electrical power of 20 W, which can represent the three types of temperature distribution. The comparison between the results from the simulation and experiments are indicated in Figure 7.

Shown in Figure 7, compared with the temperature measured by the thermal meter, the results from the thermal camera were far away from the simulated temperature. This is likely to be due to that the thermal camera had captured a superimposed temperature from both the external surface and the subsurface of the targeted composite. Therefore, the thermal camera was only applied to qualitatively validate the simulation results. On the other

hand, it can be confirmed that the temperature measured by the thermal meter were reliable for quantitative analysis of the welding process due to their good matching with the simulation results. Shown in Figure 7A–C, as to the temperature measurements by the thermal meter at the interaction surface center (ISC), the temperature was rapidly increased within the first 20 s and then gradually slowed down as the welding progressed. This phenomenon well agrees with the melting degree results in Figure 6A. However, for those measurements implemented at the top surface center (TSC), an opposite tendency was observed that the temperature slowly increased within the first 10 s, followed by a higher increasing speed.

To evaluate the simulation results, determination coefficient, R^2 ranging from 0 to 1, was used to evaluate the goodness of fit of a model and it can be calculated with the below equation:

$$R^2 = 1 - \frac{\sum (y_i - \hat{y}_i)^2}{\sum (y_i - \bar{y})^2}, \quad (8)$$

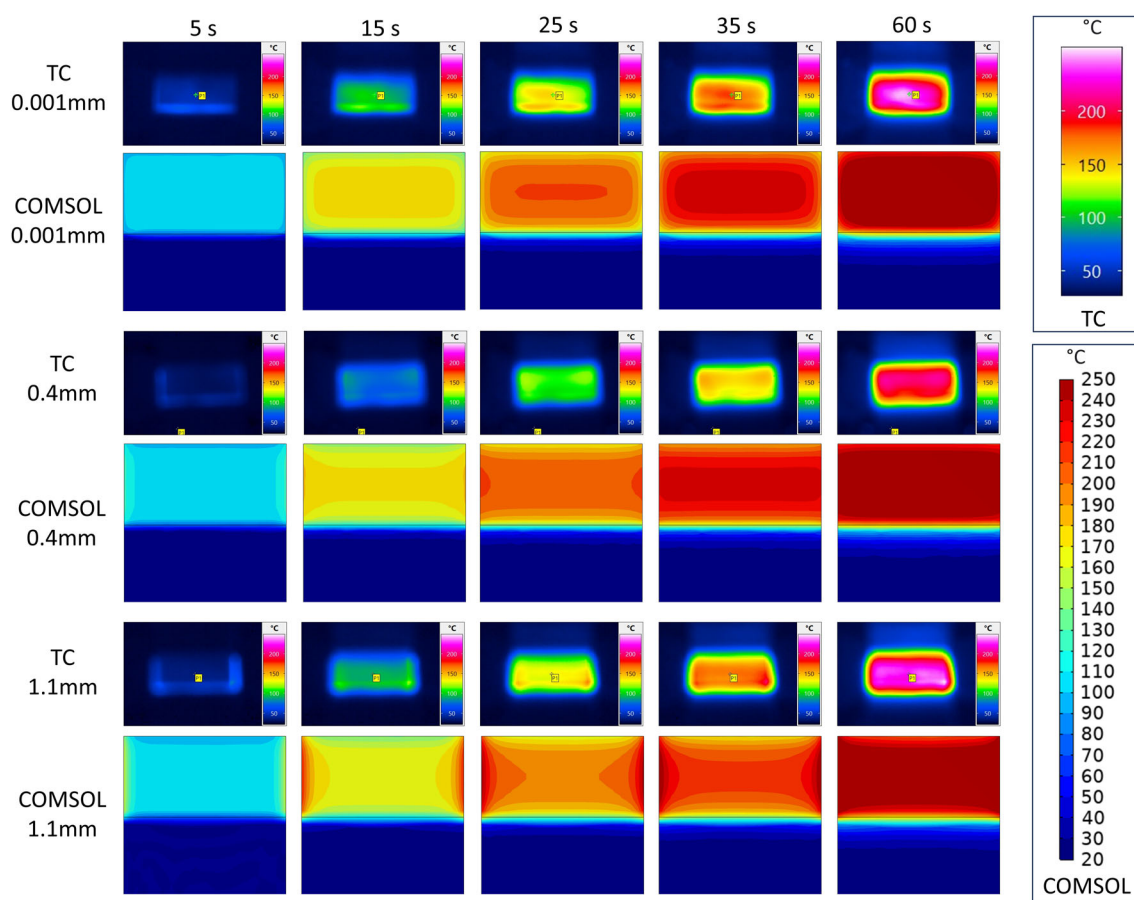


FIGURE 8 Temperature distribution maps obtained from the thermal camera (TC) and temperature contours got from COMSOL during the welding processes with different clamping distances (0.001, 0.4 and 1.1 mm) at 20 W, where 0.001 mm means zero clamping distance in reality.

where y_i , \hat{y}_i and \bar{y} measure the temperature obtained from the thermal meter, simulated temperature and average temperature measured by the thermal meter, respectively. The closer to 1 its value is, the better matching between the measured and simulated temperature more effective the above-mentioned simulation process is. The R^2 values for the simulation results at ISC were 0.943, 0.870 and 0.918 with the clamping distances of 0.001, 0.4 and 1.1 mm, respectively. Meanwhile, regarding the simulation results of TSC, the corresponding values of R^2 were 0.835, 0.916 and 0.903. All the values were nearly 1, indicating a good quantitative agreement between the simulation results and the experimental results (thermal meter).

In addition, it is noteworthy that the thermal camera can still effectively characterize the temperature distribution during the welding process for the purpose of simulation validation. The comparison between the results experimentally measured by the thermal camera and

obtained from the numerical modeling is illustrated in Figure 8. It is depicted that when the clamping distance was 0.001 mm, the temperature started increasing from the central area and the melting front (above 180°C) gradually propagated to the surrounding regions, whereas the temperature increase was initiated at two edges (left and right) which went to higher temperatures than the central area when clamping distance of 1.1 mm was used. Under clamping distance of 0.4 mm, the temperature evolution was more evenly distributed around the whole welding area, which is ideal. This finding is well aligned with the result in Figure 5, where the difference between the average temperatures along the middle line and the edge line with the clamping distance of 0.4 mm (Figure 5C) was way smaller than that with the other two, 0.001 mm (Figure 5B) and 1.1 mm (Figure 5D).

In a summary, the simulation results have been successfully validated by the experimental measurements

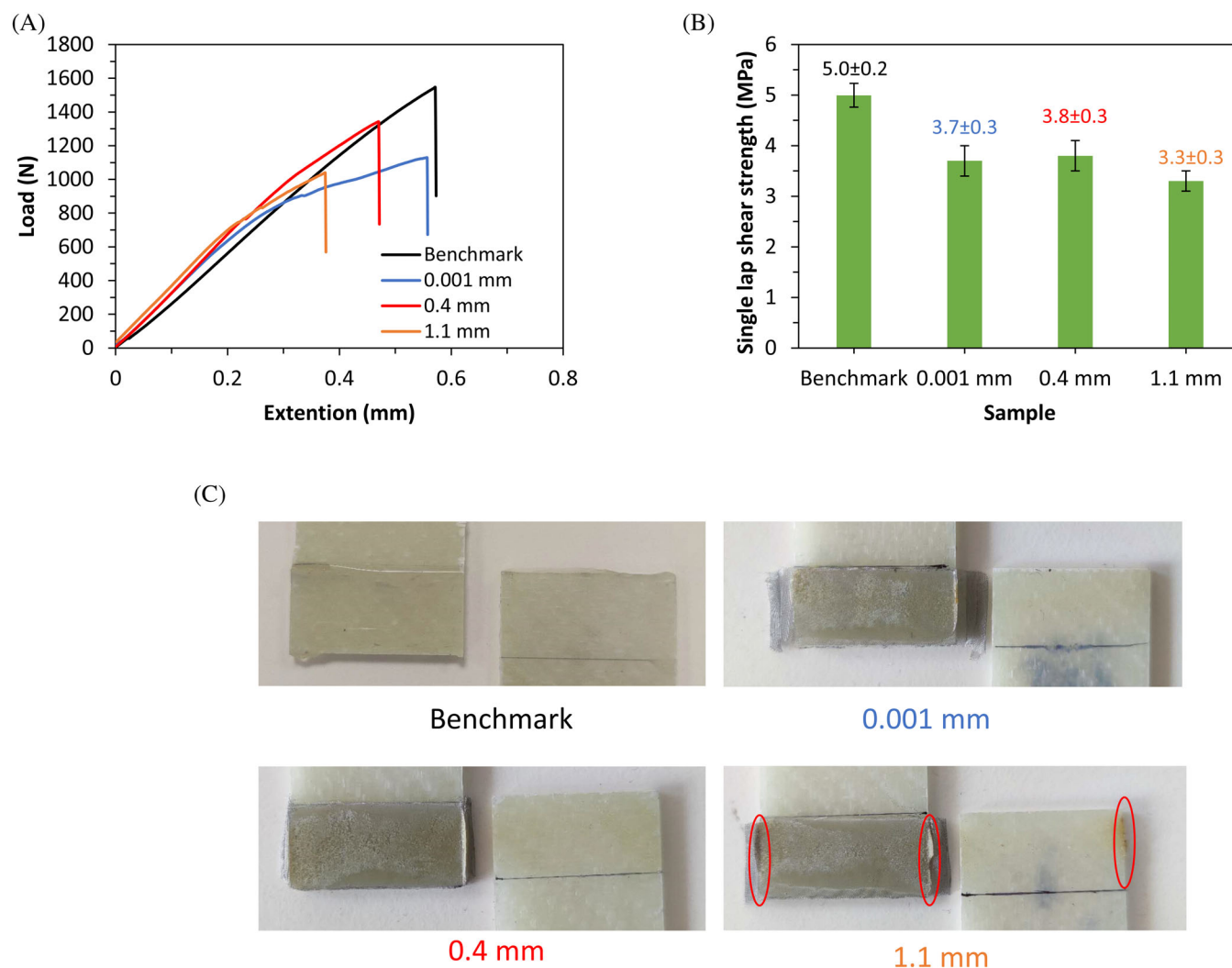


FIGURE 9 Single lap shear test results, (A) the dependence of stress as a function of extension, (B) single lap shear strength of different samples and (C) macroscopic images of failure surfaces.

assessing the heat transfer qualitatively and quantitatively with various clamping distances. The optimal power, clamping distance and welding time were eventually determined as 20 W, 0.4 mm and 30 s, respectively. The welding quality needs to be further assessed through mechanical tests, which is analyzed below.

3.3 | Evaluation of the welding quality

The single lap shear test was conducted on the samples welded at the different welding conditions where a benchmark sample made by adhesive bonding method was prepared and assessed as a reference. The single lap shear test results are shown in Figure 9.

It can be found from Figure 9A,B that among the three welding samples, the largest shear strength of 3.8 MPa was seen on the one prepared with the clamping distance of 0.4, compared with the other two, 0.001 mm, at 3.7 MPa, and 1.1 mm, at 3.3 MPa, and close to the benchmark sample made with the adhesion method (slightly lower). Consistently with what is observed in Figure 8, the distinctive edge effect (burnt line) was clearly found when the clamping distance was 1.1 mm. It suggests that the likelihood of material degradation at the edges can increase with the increase of clamping distance, which could lead to the reduction in the bonding strength, as a result of the undesired overheating zone caused by the

edge effect. Furthermore, the comparison of mechanical testing results confirmed the optimal welding conditions obtained from the numerical study.

The single lap shear strength of the welded sample was ~20% lower than that of the benchmark. The most likely reasons could be due to the residual thermal stress generated during the welding process and/or the poor adhesion between the adherent and adherend. Nevertheless, the optimized welding process was more efficient in providing specific bonding strength to the welding time than the traditional adhesion method, by over 200 times (30 s reported in this study vs. 2 hours that is found from the Elium[®] manufacturer's guide). Compared with the research conducted by Goram et al.⁴⁰ who developed the ultrasonic welding to bond carbon/Elium[®] composite and carbon/epoxy composite using a PMMA interlayer, the reported highest lap shear strength reached 7.61 MPa, which in the same level as this work presented a joining of glass fiber reinforced composite. It is also believed that a further modified formula of additive welding layer with designed pattern printed could enhance the lap shear strength as our future work.⁴¹

According to the macroscopic images of the failure surfaces shown in Figure 9C, adhesive failure seems to be the dominant failure mode, but this needs to be confirmed with other microscopic observation techniques. Therefore, SEM was conducted to evaluate the failure surfaces, and the images are shown in Figure 10.

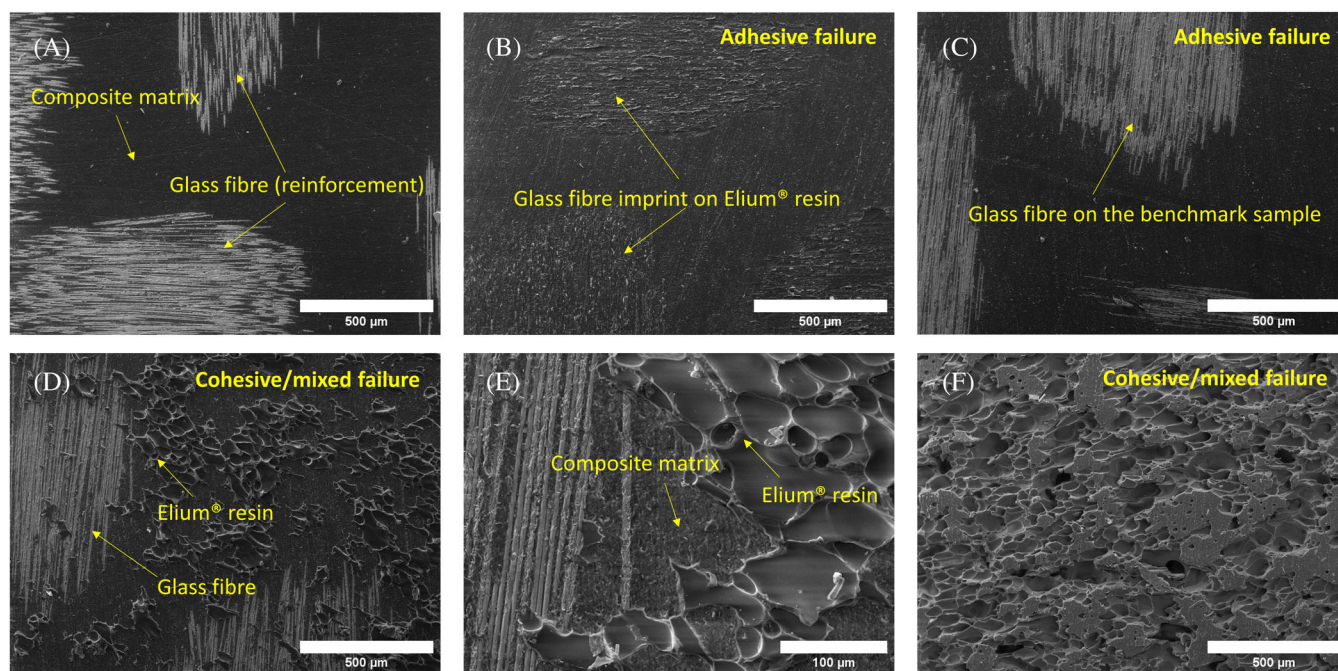


FIGURE 10 SEM micromorphological images of (A) the pristine grinded GFRC surface, (B, C) the failure surfaces of the benchmark sample, and (D, F) failure surfaces on the sample welded with the optimum condition (0.4 mm, 20 W, 30 s); the image (E) is a magnification of (D).

Compared with the pristine grinded GFRC (Figure 10A), the imprint of glass fibers was observed on one of the failure surfaces of the benchmark, with adherent (Elium[®] resin) attached, (Figure 10B) and no Elium[®] resin was found on the other failure surface of the benchmark sample (Figure 10C). This micromorphological observation proves the failure on the benchmark sample was adhesive failure, in line with the macromorphological observation in Figure 9C. As for the sample prepared with the optimum welding process, there were adherent (Elium[®] resin) lumps observed on one failure surface with the composite matrix and glass fiber exposed, see Figure 10D,E. Meanwhile, on the other side of the failure surface of the welded sample (Figure 10F), imprint of the lumps was seen, which proves that the microscopic failure mode of the welded sample was cohesive/mixed failure. The microscopic failure mode of the welded sample is misaligned with the macroscopic one and is determined as the true failure mode. However, the observed microscopic failure mode does not align with the lap shear testing results that the bonding strength of the benchmark sample should be worse than that of the welded sample with the optimal conditions. The reason is likely to be that the thermal stress induced at the joint surface of the welded sample compromised the interfacial bonding quality along the joint line upon the resistance welding process. Therefore, optimizing the design of the heating element to further increase the thermal distribution, especially along the longitudinal direction of the joint area (refer to the coordinate system illustrated in Figure 2B), could be one of the prospects.

4 | CONCLUSIONS

The resistance welding process of the glass fiber reinforced-epoxy composite with a self-prepared Elium[®] film and a steel mesh has been successfully investigated. The parametric optimization study on the resistance welding process was conducted with the transient heat transfer module in COMSOL Multiphysics. The GFRC used in this study was measured to be isotropic in thermal conductivity upon comparison between the numerical and experimental results, and this is in line with the literature.³⁸ The thermal degradation temperatures of the Elium[®] film and GFRC were tested to be 250 and 287°C, using TGA, respectively. The examination of the effect of electricity power on the welding process showed that the higher the power was, the faster type (3) temperature distribution achieved, where the average temperature at type (3) distribution increased from 158 to 322°C with the power from 15 to 30 W. The optimal power for the welding process was preliminarily confirmed to be 20 W with the type (3) average temperature of 245°C. The further numerical optimization process

confirmed the optimal welding condition with the clamping distance, power and welding time to be 0.4 mm, 20 W and 30 s, respectively. These heat transfer results were successfully validated with a thermal meter and a thermal camera. In addition, to evaluate the welding quality, single lap shear tests and SEM were implemented to study the mechanical properties and micromorphology of the welded specimens. The highest single lap shear strength was seen on the sample welded with the above-mentioned optimal welding condition, at 3.8 MPa, which is just about 20% lower than the benchmark prepared with the adhesive bonding method, at 5.0 MPa. With the assistance of SEM observation, the reason is hypothesized to be the uneven temperature distribution along the longitudinal direction of the welding area after the comparison in failure surface between the benchmark and the sample welded with the optimal welding process. To further improve the temperature distribution especially along the longitudinal direction, investigation on designing the heating elements is proposed to be a solution. Nevertheless, compared with the adhesive bonding method, the optimized welding process is over 200 times faster, giving a higher specific lap shear strength to the time needed for the joining. The findings in this paper provide informative knowledge to the researchers and engineers working in the field of joining thermoset-based composites with thermoplastic polymers.

ACKNOWLEDGMENTS

The research leading to this paper is part of the Romain project that has received funding from the European Union's Horizon Europe research and innovation programme under grant agreement No. 101070320. UK participants are supported by UKRI grant number [10101311] (University of Leeds). The simulation work was undertaken on ARC4, part of the High Performance Computing facilities at the University of Leeds, UK. The authors would also like to thank the mechanical engineering team at the University of Chester.

DATA AVAILABILITY STATEMENT

Data are available on request from the authors.

ORCID

Yunhao Liang  <https://orcid.org/0000-0003-0552-1297>

REFERENCES

1. Gibson RF. A review of recent research on mechanics of multi-functional composite materials and structures. *Compos Struct*. 2010;92(12):2793-2810.
2. Hale DK. The physical properties of composite materials. *J Mater Sci*. 1976;11(11):2105-2141. doi:10.1007/PL00020339
3. Bakis CE, Bank LC, Brown VL, et al. Fiber-reinforced polymer composites for construction - state-of-the-art review. *Perspectives*

- in *Civil Engineering: Commemorating the 150th Anniversary of the American Society of Civil Engineers*. Vol 6. American Society of Civil Engineers; 2003:369-383. doi:[10.1061/\(asce\)1090-0268\(2002\)6](https://doi.org/10.1061/(asce)1090-0268(2002)6)
4. Hsissou R, Seghiri R, Benzekri Z, Hilali M, Rafik M, Elharfi A. Polymer composite materials: a comprehensive review. *Compos Struct*. 2021;262:113640. doi:[10.1016/j.compstruct.2021.113640](https://doi.org/10.1016/j.compstruct.2021.113640)
 5. Saheb DN, Jog JP. Natural fiber polymer composites: a review. *Adv Polym Technol*. 1999;18(4):351-363. doi:[10.1002/\(SICI\)1098-2329\(199924\)18:43.0.CO;2-X](https://doi.org/10.1002/(SICI)1098-2329(199924)18:43.0.CO;2-X)
 6. Tian L, Zhang P, Xian G. Continuous fiber reinforced thermoplastic composite pultrusion with in situ polymerizable methyl methacrylate: a review. *Polym Compos*. 2023;44(8):4345-4369. doi:[10.1002/PC.27427](https://doi.org/10.1002/PC.27427)
 7. Xiong X, Wang D, Wei J, et al. Resistance welding technology of fiber reinforced polymer composites: a review. *J Adhes Sci Technol*. 2021;35(15):1593-1619. doi:[10.1080/01694243.2020.1856514](https://doi.org/10.1080/01694243.2020.1856514)
 8. Kempe G, Krauss H, Korger-Roth G. Adhesion and welding of continuous carbon-fiber reinforced polyether Etherketone (CF-PEEK/APC2). *Developments in the Science and Technology of Composite Materials*. Springer; 1990:105-112. doi:[10.1007/978-94-009-0787-4_12](https://doi.org/10.1007/978-94-009-0787-4_12)
 9. Liu A, Zou Y, Chen Y, Hu J, Wang B. Experimental investigation of impact resistance and compression behavior of CF/PEEK laminates after hot-press fusion repair with different stacking sequences. *Polym Compos*. 2023;44(10):6467-6481. doi:[10.1002/PC.27571](https://doi.org/10.1002/PC.27571)
 10. Novakovic B, Kashkoush M. Modeling the matching stage of HDPE hot plate welding: a study using regression and support vector machine models. *Polym Eng Sci*. 2023;1-18. doi:[10.1002/PEN.26587](https://doi.org/10.1002/PEN.26587)
 11. Villegas IF. Ultrasonic welding of thermoplastic composites. *Front Mater*. 2019;6:6. doi:[10.3389/fmats.2019.00291](https://doi.org/10.3389/fmats.2019.00291)
 12. Wang Y, Rao Z, Liao S, Wang F. Ultrasonic welding of fiber reinforced thermoplastic composites: current understanding and challenges. *Compos Part A Appl Sci Manuf*. 2021;149:106578. doi:[10.1016/j.compositesa.2021.106578](https://doi.org/10.1016/j.compositesa.2021.106578)
 13. Benatar A, Gutowski TG. Ultrasonic welding of PEEK graphite APC-2 composites. *Polym Eng Sci*. 1989;29(23):1705-1721. doi:[10.1002/pen.760292313](https://doi.org/10.1002/pen.760292313)
 14. Cosson B, Deléglise M, Knapp W. Numerical analysis of thermoplastic composites laser welding using ray tracing method. *Compos Part B Eng*. 2015;68:85-91. doi:[10.1016/j.compositesb.2014.08.028](https://doi.org/10.1016/j.compositesb.2014.08.028)
 15. Zhang Z, Zhao H, Zhao Y, et al. Effect of surface texture spacing on interface heat transfer and tensile property of laser-welded steel/CFRTP joint. *Polym Compos*. 2024;45(2):1551-1567. doi:[10.1002/PC.27873](https://doi.org/10.1002/PC.27873)
 16. Kagan VA, Nichols RJ. Benefits of induction welding of reinforced thermoplastics in high performance applications. *J Reinf Plast Compos*. 2005;24(13):1345-1352. doi:[10.1177/0731684405048846](https://doi.org/10.1177/0731684405048846)
 17. Davies P, Cantwell WJ, Jar PY, Bourban PE, Zysman V, Kausch HH. Joining and repair of a carbon fibre-reinforced thermoplastic. *Composites*. 1991;22(6):425-431. doi:[10.1016/0010-4361\(91\)90199-Q](https://doi.org/10.1016/0010-4361(91)90199-Q)
 18. Hou M, Ye L, Mai YW. An experimental study of resistance welding of carbon fibre fabric reinforced polyetherimide (CF fabric/PEI) composite material. *Appl Compos Mater*. 1999;6(1):35-49. doi:[10.1023/A:1008879402267](https://doi.org/10.1023/A:1008879402267)
 19. Zhang G, Lin T, Luo L, Zhang B, Qu Y, Meng B. Multi-objective optimization of resistance welding process of gf/pp composites. *Polymers (Basel)*. 2021;13(15):2560. doi:[10.3390/polym13152560](https://doi.org/10.3390/polym13152560)
 20. Li X, Zhang T, Li S, Liu H, Zhao Y, Wang K. The effect of cooling rate on resistance-welded CF/PEEK joints. *J Mater Res Technol*. 2021;12:53-62. doi:[10.1016/j.jmrt.2021.02.071](https://doi.org/10.1016/j.jmrt.2021.02.071)
 21. Iqbal Z, Siddique A, Nawab Y, Shaker K. A comparative static and dynamic behavior of thermoplastic composite joints produced using different joining techniques. *Polym Compos*. 2023;44(8):4853-4861. doi:[10.1002/PC.27448](https://doi.org/10.1002/PC.27448)
 22. Ageorges C, Ye L, Mai YW, Hou M. Characteristics of resistance welding of lap shear coupons: part II. Consolidation. *Compos Part A Appl Sci Manuf*. 1998;29(8):911-919. doi:[10.1016/S1359-835X\(98\)00023-2](https://doi.org/10.1016/S1359-835X(98)00023-2)
 23. Shi H, Villegas IF, Octeau MA, Bersee HEN, Yousefpour A. Continuous resistance welding of thermoplastic composites: modelling of heat generation and heat transfer. *Compos Part A Appl Sci Manuf*. 2015;70:16-26. doi:[10.1016/j.compositesa.2014.12.007](https://doi.org/10.1016/j.compositesa.2014.12.007)
 24. Brøndsted P, Lilholt H, Lystrup A. Composite materials for wind power turbine blades. *Annu Rev Mater Res*. 2005;35:505-538. doi:[10.1146/annurev.matsci.35.100303.110641](https://doi.org/10.1146/annurev.matsci.35.100303.110641)
 25. Katnam KB, Comer AJ, Roy D, Da Silva LFM, Young TM. Composite repair in wind turbine blades: an overview. *J Adhes*. 2015;91(1-2):113-139. doi:[10.1080/00218464.2014.900449](https://doi.org/10.1080/00218464.2014.900449)
 26. Gomez CM, Bucknall CB. Blends of poly(methyl methacrylate) with epoxy resin and an aliphatic amine hardener. *Polymer (Guildf)*. 1993;34(10):2111-2117. doi:[10.1016/0032-3861\(93\)90737-U](https://doi.org/10.1016/0032-3861(93)90737-U)
 27. Janarthanan V, Thyagarajan G. Miscibility studies in blends of poly(N-vinyl pyrrolidone) and poly(methyl methacrylate) with epoxy resin: a comparison. *Polymer (Guildf)*. 1992;33(17):3593-3597. doi:[10.1016/0032-3861\(92\)90641-9](https://doi.org/10.1016/0032-3861(92)90641-9)
 28. Khan T, Ali MA, Irfan MS, Cantwell WJ, Rehan U. Visualizing pseudo-ductility in carbon/glass fiber hybrid composites manufactured using infusible thermoplastic Elium® resin. *Polym Compos*. 2023;44(3):1859-1876. doi:[10.1002/PC.27210](https://doi.org/10.1002/PC.27210)
 29. ASTM D1002. *Standard Test Method for Apparent Shear Strength of Single-Lap-Joint Bonded Metal Specimens by Tension Loading (Metal-to-Metal)*. ASTM International; 2005.
 30. Ageorges C, Ye L, Mai YW, Hou M. Characteristics of resistance welding of lap shear coupons. Part I: heat transfer. *Compos Part A Appl Sci Manuf*. 1998;29(8):899-909. doi:[10.1016/S1359-835X\(98\)00022-0](https://doi.org/10.1016/S1359-835X(98)00022-0)
 31. Holmes ST, Gillespie JW. Thermal analysis for resistance welding of large-scale thermoplastic composite joints. *J Reinf Plast Compos*. 1993;12(6):723-736. doi:[10.1177/073168449301200609](https://doi.org/10.1177/073168449301200609)
 32. Talbot É, Hubert P, Dubé M, Yousefpour A. Optimization of thermoplastic composites resistance welding parameters based on transient heat transfer finite element modeling. *J Thermoplast Compos Mater*. 2013;26(5):699-717. doi:[10.1177/0892705711428657](https://doi.org/10.1177/0892705711428657)
 33. PAR Group Ltd. Sindanyo® H91 Technical Data Sheet.
 34. Muthuraj R, Grohens Y, Seantier B. Mechanical and thermal insulation properties of elium acrylic resin/cellulose nanofiber based composite aerogels. *Nano-Struct Nano-Objects*. 2017;12:68-76. doi:[10.1016/J.NANOSO.2017.09.002](https://doi.org/10.1016/J.NANOSO.2017.09.002)
 35. Polymethylmethacrylate (PMMA, Acrylic) material properties. Accessed December 7, 2023 <https://web.archive.org/web/>

- 20150402124133/http://www.makeitfrom.com/material-properties/Polymethylmethacrylate-PMMA-Acrylic
36. Atlas Specialty Metals Technical Services Department. The Atlas Specialty Metals Technical Handbook of Stainless Steels; 2003.
 37. ASM Material Data Sheet. Accessed December 7, 2023 <https://asm.matweb.com/search/SpecificMaterial.asp?bassnum=mq304a>
 38. Takizawa Y, Chung DDL. Through-thickness thermal conduction in glass fiber polymer-matrix composites and its enhancement by composite modification. *J Mater Sci.* 2016; 51(7):3463-3480. doi:10.1007/s10853-015-9665-x
 39. Stavrov D, Bersee HEN. Resistance welding of thermoplastic composites-an overview. *Compos Part A Appl Sci Manuf.* 2005; 36(1):39-54. doi:10.1016/j.compositesa.2004.06.030
 40. Gohel G, Soh CZ, Leong KF, Gerard P, Bhudolia SK. Effect of PMMA coupling layer in enhancing the ultrasonic weld strength of novel room temperature curable acrylic thermoplastic to epoxy based composites. *Polymers (Basel).* 2022;14(9):1862. doi:10.3390/polym14091862

41. Shi Y, Wang X, Wang F, Gu T, Xie P, Jia Y. Effects of inkjet printed toughener on delamination suppression in drilling of carbon fibre reinforced plastics (CFRPs). *Compos Struct.* 2020; 245:112339.

SUPPORTING INFORMATION

Additional supporting information can be found online in the Supporting Information section at the end of this article.

How to cite this article: Liang Y, Shi Y. Computational and experimental study on the resistance welding process of a glass fiber-reinforced epoxy-based composite with thermoplastic interlayer adherent. *Polym Compos.* 2024;45(6):5096-5110. doi:10.1002/pc.28113